Yi Jiang | Ulrich Mansfeld | Liang Fang | Karl Kratz | Andreas Lendlein

Temperature-induced evolution of microstructures on poly[ethylene-co-(vinyl acetate)] substrates switches their underwater wettability

Temperature-induced evolution of microstructures on poly[ethylene-co-(vinyl acetate)] substrates switches their underwater wettability

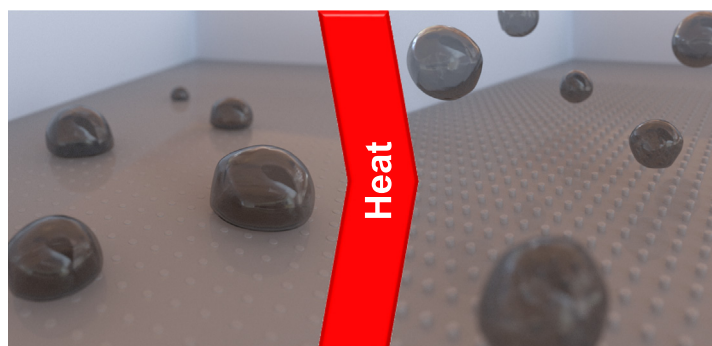Yi Jiang [a,b], Ulrich Mansfeld [a], Liang Fang [a,1], Karl Kratz [a], Andreas Lendlein [a,b,*]

[a] Institute of Biomaterial Science, Helmholtz-Zentrum Geesthacht, Kantstr. 55, 14513 Teltow, Germany
[b] Institute of Chemistry, University of Potsdam, Karl-Liebknecht-Str. 24-25, 14476 Potsdam, Germany

HIGHLIGHTS

- Hydrophobic polymer substrates comprising microcylinders exhibit underwater repellence of approaching air bubbles.
- Upon heating, temporarily flat, aerophilic substrates change to microstructured substrates that show aerophobic behavior.
- The change in underwater wettability is caused by entrapment of a water film between the microstructures.
- An excellent temperature-memory performance was shown on micro- and nanoscale for the presented polymer substrates.
- The temperature at which the air bubble repellence occurs can be controlled by the deformation temperature applied.

GRAPHICAL ABSTRACT

ARTICLE INFO

ABSTRACT

Material surfaces with tailored aerophobicity are crucial for applications where gas bubble wettability has to be controlled, e.g., gas storage and transport, electrodes, bioreactors or medical devices.

Here, we present switchable underwater aerophobicity of hydrophobic polymeric substrates, which respond to heat with multilevel micro- and nanotopographical changes. The cross-linked poly[ethylene-co-(vinyl acetate)] substrates possess arrays of microcylinders with a nanorough top surface. It is hypothesized that the specific micro-/nanotopography of the surface allows trapping of a water film at the micro interspace and in this way generates the aerophobic behavior. The structured substrates were programmed to a temporarily stable, nanoscale flat substrate showing aerophilic behavior. Upon heating, the topographical changes caused a switch in contact angle from aerophilic to aerophobic for approaching air bubbles. In this way, the initial adhesion of air bubbles to the programmed flat substrate could be turned into repellence for the recovered substrate surface. The temperature at which the repellence of air bubbles starts can be adjusted from 58 ± 3 °C to 73 ± 3 °C by varying the deformation temperature applied during the temperature-memory programming procedure. The presented actively switching polymeric substrates are attractive candidates for applications, where an on-demand gas bubble repellence is advantageous.

1. Introduction

Controlling gas bubble wettability of advanced materials (i.e. metals or polymers) in aqueous media is a major technological challenge and of great relevance for many applications, e.g. gas storage and transport, electrodes, sensors or medical devices [1–2]. The wettability on a material surface is governed by the relation of the interfacial tensions for a ternary system (gas/water/material) representing minimal Gibbs free energy [3]. Besides the chemical composition at the material surface, the topographical surface design on micro- and nanoscale alters the wettability and can be utilized to gain, e.g., superwettability [4–5]. In this context, the increase of micro- and nano roughness on surfaces typically results in an increase in hydrophilicity or hydrophobicity towards superwetting, when the solid substrate is fully in contact with water in the so called Wenzel state [6] or when air is entrapped by the surface topography underneath the water in Cassie state [7], hereby the contact lines are of great importance [8]. Along these minimal free energy considerations, in particular hierarchically micro/nanostructured (super) hydrophilic surfaces exhibit (super)aerophobicity and (super)hydrophobic surfaces are (super)aerophilic [2,9–14].

However, real surfaces can exhibit metastable states of local energy minima resulting in novel combinations of wettability [3]. Examples are, e.g., natural rose petal surfaces [15] and laser-patterned PDMS surfaces [16] with hierarchical nano- and microstructures, showing hydrophobicity in combination with aerophobic behavior upon the attachment of air bubbles underwater. Besides static bubble wettability of micro-/nanostructured materials, a switchable underwater superaerophobicity was recently reported for nanowired-haired copper meshes, when a specific vacuuming procedure was applied [17]. Another recent work describes switchable underwater bubble wettability of micro- and nanostructured titanium oxide after heat treatment or UV irradiation in alcohol, which is attributed to a change in surface chemistry between Ti-OH and Ti-O [18].

Alternatively, responsive soft polymeric surfaces, that can actively change their micro/nanotopography upon external stimuli, also have the potential to dynamically switch surface functions [19–21]. In this context, the switching of surface functions such as wettability, controlled by shape-memory effects of polymeric surfaces has been reported as a working principle [22–29]. Here micro- or nanotopographical changes on the polymer surface were realized by exposing programmed polymers to temperatures above their switching temperature (related to a thermal transition of the polymer material), whereby the original shape is recovered [30–34]. For programming, typically a heating-deformation-cooling procedure is applied. Programming of microstructured polymer surfaces is typically realized by vertical compression with flat or structured molds or via stretching the specimen laterally [23,25]. In this context various microtopographical shape changes in polymers have been realized [22–28,35–36]. Polymer networks having a broad melting or glass transition can be programmed to show a temperature-memory effect. Here, the deformation applied for programming is performed at temperatures within the thermal transition, allowing the adjustment of the switching temperature by solely variation of the deformation temperature [37–42].

Poly[ethylene-*co*-(vinyl acetate)] (PEVA) copolymers are thermoplastic materials of high application relevance in various fields e.g. as packaging films, adhesives, coatings/resins, additives/fillers for construction materials, damping foams, membrane technologies and drug release systems, because their properties can be adjusted in a wide range by variation of their composition in particular the ethylene to vinyl acetate ratio [43–46]. PEVA copolymers were initially developed to substitute soft polyvinyl chloride polymers (PVC), which require the utilization of plasticizer for meeting the application demanded mechanical properties. PEVA copolymers are hydrophobic materials, which have a relatively low water absorption capacity [46–49]. In this context, contact angles in the range of 88° to 97° have been reported for PEVA films with a vinyl acetate content of 18 wt-% and different roughness [48]. Crosslinked PEVA materials can exhibit macroscopic as well as microscopic shape-memory effects, whereby the crystallizable polyethylene domains are utilized as switching or actuating units [36–37,41,50–53].

We hypothesize that the temperature-memory capability of hydrophobic polymeric substrates with a specifically designed micro/nanosurface structure can be utilized to create a significant switch from aerophilic (air bubble attaching) to aerophobic (air bubble repellent) at tailorable temperatures. Hereby, the resultant aerophobic state is based on the trapping of water between the recovered surface structure and an approaching air bubble. The stability of the water film should mainly depend on the recovered micro-feature height and may be supported by associated nano-topographical changes (Scheme 1).
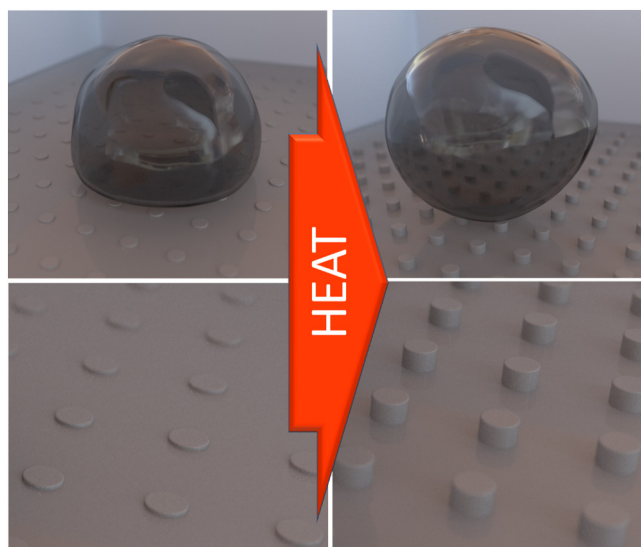
The system concept is based on microstructured crosslinked poly [ethylene-*co*-(vinyl acetate)] substrates (cPEVA) with a vinyl acetate content of 18 wt-%. The topographical design of the cPEVA substrate surface consisted of an array microcylinders (diameter 25 μm, height 10 μm) having a specific nanoroughness (S_a ~10 nm) on top of the cylinders, while the interspace (50 μm) was nanosmooth (S_a < 1 nm). The interspace/cylinder height ratio is chosen to allow for water wetting, but also ensure water trapping upon air bubble contact.

Our strategy involves the generation of temporarily "flat" cPEVA substrates by vertical compression of the microcylinders into the surface utilizing a temperature-memory creation procedure. Such flattened surfaces should provide an underwater aerophilic behavior (attachment of bubbles) due to the intrinsic hydrophobic nature of cPEVA. When heating the temporarily flat substrates, the recovery of the microcylinders will occur at temperatures similar to that applied during TME programming, which should result in underwater aerophobic behavior of the substrate based on the water trapping at the surface feature interspace. To quantitatively evaluate the Temperature Memory Effect (TME) on the micro- and nanoscale, the shape recovery is followed by atomic force microscopy (AFM). The temperature dependent aerophobicity switch and resulting air bubble repellence are investigated by captive bubble related methods.

2. Experimental section

2.1. Materials

Poly[ethylene-*co*-(vinyl acetate)] (PEVA) with a vinyl acetate content of 18 wt% (trade name: Elvax460) was obtained from DuPont de

Scheme 1. Schematic representation of the thermally-induced recovery of microcylinders on a temporarily flat programmed polymeric substrate), that upon heating, switches from attaching to approaching underwater air bubbles (aerophilic behaviour), to repelling the approaching air bubbles (aerophobic behaviour).

Nemours (Neu-Isenburg, Germany). Crosslinking agent dicumyl peroxide and toluene (99.8%) used for solution casting and gel content measurement were purchased from Sigma-Aldrich (Sigma-Aldrich Chemie GmbH, Taufkirchen, Germany). Sylgard 184 silicone elastomer kit, used to prepare poly(dimethylsiloxane) (PDMS) molds, was manufactured by Dow Corning (Dow Corning Corp. Midland, MI, USA). All chemicals were used as received. Smooth and custom-made microstructured Si-wafers containing arrays of cylindrical micro-wells with 25 μm, interspaces of 50 μm, and depth of 10 μm were purchased from IMS CHIPS (Stuttgart, Germany).

2.2. Preparation of cPEVA substrates

The microstructured crosslinked poly[ethylene-co-(vinyl acetate)] films (cPEVA) were prepared by soft lithography and crosslinking according to the method described in literature [36]. Flat cPEVA films were prepared accordingly by using a flat PDMS mold that was replicated from a smooth silicon wafer. In order to erase the thermomechanical history originating from the cPEVA substrate preparation, all cPEVA substrates were pretreated at 100 °C for 10 min in a thermo-oven (Vacutherm, Heraeus, Hanau, Germany) followed by cooling to 10 °C for 20 min prior further programming or investigations.

2.3. Temperature-memory programming

The microstructured cPEVA substrates were programmed by vertical compression similar to the previously reported protocol [36]. In brief, the microstructured substrate (0.5 cm × 0.5 cm) was placed between two smooth silicon wafers and compressed by using foldback clips (width 25 mm) at a certain T_{prog} between 40 °C and 100 °C for 20 min and subsequent fixation at 10 °C for another 20 min prior pressure release. The compression force of the applied foldback clips was measured to be around 20 N. The samples used for contact angle measurement required a larger area (2 cm × 2 cm) and thus a higher compression force to maintain the same pressure on the sample. Therefore, a compression machine type 200 E (Dr. Collin, Ebersberg, Germany) was used to ensure the same pressure on the samples.

2.4. Optical microscopy

Digital microscopy experiments were carried out on a VHX-Z500 digital microscope (OM, VHX-100K, Keyence Cor., Osaka, Japan) to observe the topography of microstructured surface. For in-situ observation during the recovery process, an external Cooler/Heater (Asylum Research, Goleta, USA) was equipped to control the real-time temperature of the sample. The heating rate was 10 °C·min^{-1}, and the samples were equilibrated at each investigated temperature for 10 min before observation.

2.5. Atomic force microscopy

Atomic force microscopy (AFM) measurements at various temperatures were performed on a MFP-3D-BioTM AFM (Asylum Research, Goleta, USA) equipped with a Cooler/Heater controller (Asylum Research, Goleta, USA) according to the method reported before [36]. The applied heating rate was 10 °C·min^{-1} and the samples were equilibrated at each investigated temperature for 10 min before measurement. AC mode with a scan rate of 0.5 Hz was applied to characterize the topographies of single microcylinders. The probe type AC200TS (Olympus, Tokyo, Japan) with a typical driving frequency of 150 kHz (individual difference ranged from 100 to 200 kHz) and a typical spring constant of 9 N·m^{-1} (individual difference ranged from 2.8 to 21 N·m^{-1}) was used. The tip radius and height are respective 5–10 nm and 14 ± 1 μm. The tip was three-side shaped with a front angle of 0 ± 1°, a back angle of 35 ± 1°, and a side angle of 15 ± 1°. A scan size of 50 μm × 50 μm was chosen for investigation of the

individual microcylinders' height and diameter. The apparent height H determined by AFM represents the height of the microcylinders relative to the level of the surrounding interpillar surface of the substrate. Five individual microcylinders were analyzed for determination of the average apparent height H. Three-dimensional AFM image representations of the obtained raw data (height images and surface roughness) were processed with the software MountainsMap® (Digital Surf, Besançon, France).

The roughness of the cylinder's top surface can be characterized by the area surface roughness (S_a) of a surface area (A) according to EN ISO 25178 which is defined by the difference of the height of each surface point z(x,y) to the arithmetical mean height of a surface given by the following equation:

$$S_a = \frac{1}{A}\iint\limits_A |z(x,y)|dxdy \tag{1}$$

For determination of S_a an area of 10μm × 10 μm in the center of the microcylinder top surface was analyzed for five individual cylinders.

The apparent shape deformation ratio $R_{d,\mu}$, fixation ratio ($R_{f,\mu}$) and recovery ratio $R_{r,\mu}$ of single microcylinders could be calculated according to:

$$R_{d,\mu} = \frac{H_0-H_\mu}{H_0}\times 100\%; \quad R_{f,\mu} = \frac{H_0-H_\mu}{H_0-H_{Tp}}\times 100\% \tag{2}$$

$$R_{r,\mu} = \frac{H-H_\mu}{H_0-H_\mu}\times 100\% \tag{3}$$

with H_0 and H_μ being the apparent heights of original and temporary microcylinders, respectively, and H is the apparent height of programmed microcylinders at a certain temperature during the recovery process. In case the cylinder is compressed to zero height ($H_{Tp} = 0$ μm) in relation to the surrounding surface level upon compression, $R_{d,\mu}$ equals $R_{f,\mu}$.

The top surface (nano)roughness deformation ratio ($R_{d,n}$) and recovery ratio ($R_{r,n}$) could be calculated according to:

$$R_{d,n} = \frac{S_{a,0}-S_{a,\mu}}{S_{a,0}}\times 100\% \tag{4}$$

$$R_{r,n} = \frac{S_a-S_{a,\mu}}{S_{a,0}-S_{a,\mu}}\times 100\% \tag{5}$$

with $S_{a,0}$ and $S_{a,\mu}$ being cylinder top area surface roughness of original and temporary microcylinders, respectively, and S_a is the top area surface roughness of programmed microcylinders at a certain temperature during the recovery process.

2.6. Scanning electron microscopy

The samples were observed at room temperature using a scanning electron microscopy (SEM) Gemini Supra 40 VP (Zeiss, Oberkochen, Germany) equipped with an in-lens detector at 2 kV and 3 kV. The samples were cut prior the investigation with a razor blade at room temperature and were inspected without coating.

2.7. Dynamic contact angle measurements

Dynamic contact angle (dCA) measurements were carried out using a drop shape analyzer (DSA 100, Krüss GmbH, Hamburg, Germany). For the measurements ultra-pure deionized water provided by an Ultra Clear UV clean water system (SG Wasseraufbereitung und Regenerierstation GmbH, Barsbüttel, Germany) with a conductivity of 0.055 μS/cm was used. The sessile drop method was used to characterize the samples at room temperature. For in-situ temperature experiments the captive

bubble method was used. The sample was mounted into a deionized water reservoir with the structured side facing down and the air bubbles were delivered via a U-shaped needle. The temperature could be varied in the range from 25 °C and 75 °C with the current setup. The water was heated up stepwise and the sample equilibrated 10 min prior measurement. The contact area between the surface and the bubble was increased with each measurement cycle from 2 to 5 mm in diameter. In order to make a full recovery, all programmed samples were finally heated up to 100 °C and equilibrated for 10 min and contact angles (CA) were measured at 25 °C and 75 °C. At least ten measurements were performed for each sample.

2.8. Dynamic micro contact angle determination by environmental scanning electron microscopy

The microscale wetting behavior of structured cPEVA substrates was investigated at 2 °C by environmental scanning electron microscopy (ESEM) using a Quanta FEG 250 (FEI, Eindhoven, The Netherlands) operating at 30 kV equipped with a gaseous secondary electron detector. The uncoated sample was observed parallel to the cylinder's top surfaces and the advancing CAs of condensing water droplets on top and in between cylinders were measured at a chamber pressure of 780 Pa. At least ten measurements of advancing angle were performed for each sample.

2.9. In-situ air bubble repellence experiments

To demonstrate the air bubble adhesion to repellence change, which goes along with the temperature-memory effect, a modified captive air bubble method was used. The sample was mounted into a deionized water reservoir with the structured side facing upwards and air bubbles were allowed to attach to the surface from a distance of 0.5 to 2 mm. The temperature could be varied in the range from 25 °C to 75 °C with the current setup. For the in-situ attachment measurement, the water was heated stepwise to the desired temperatures and the sample was allowed to equilibrate for 10 min after each step prior the attachment of air bubbles. For each temperature, at least 5 measurements were repeated at different locations of the film and the dynamic process was recorded as movies.

2.10. Descriptive statistics and error consideration

The data presented in this study are average values with respective standard deviations based on at least five independent measurements, unless stated otherwise.

3. Results and discussion

Microstructured cPEVA substrates with a vinyl acetate content of 18 wt-% comprising cylindrical microcylinders with a diameter of 25 μm, a height of 10 μm and the interspaces of 50 μm were fabricated via an integrated structuring technique [36].

3.1. Characteristics of unprogrammed cPEVA films

A successful almost complete crosslinking of the thermoplastic starting material by the integrated structuring approach was confirmed by a high gel content of $93 \pm 1\%$ determined in swelling/deswelling experiments with toluene (see SI Experimental). Thermal properties of the cPEVA films were investigated by differential scanning calorimetry (DSC) (SI Experimental, Fig. S1) showing a broad melting transition temperature in the first heating run that ranges from 15 °C to 90 °C with a peak maximum at 80 °C. The integrated melting enthalpy of $\Delta H_m = 68 \pm 1\,J \cdot g^{-1}$ corresponds to a degree of crystallization (DOC) of $23 \pm 1\%$. A complete melting was observed above 90 °C. Upon cooling, a crystallization peak at 57 °C was obtained. Based on the

broad melting transition the programming temperatures (T_{prog}) were chosen in the range of 40 to 100 °C to investigate the influence on the resultant temporarily flat substrates (Section 3.3) and the temperature-induced shape recovery behavior (Section 3.4). A fixation temperature of 10 °C was chosen to ensure proper crystallization. The prepared microstructured cPEVA films were investigated by optical microscopy showing uniform distribution of microcylinders over large areas matching the diameter (25 μm) and spacing (50 μm) dimensions of the complementary poly(dimethylsiloxane) (PDMS) mold suggesting a successful micro-patterning (Fig. S2). The uniformity of the microcylinders was visualized by SEM showing arrays of identical cylinders with an average height of 10.0 ± 0.1 μm over a large substrate area (Fig. 1a). AFM was chosen as a noninvasive method to investigate single microcylinders on micro- and nanoscale. Beside micro-scale characterization of the cylinders as already reported elsewhere [36] (Fig. 1b, c and Table 1), the nanoroughness on cylinders' top surface and of the interspacing surface was measured by AFM revealing a surface roughness of $S_a = 10 \pm 1$ nm (Fig. 1e) and $S_a < 1$ nm (Fig. 1d), respectively. For details on the calculation of the nanoroughness S_a from height images see Eq. (1). This nanoroughness is caused by the etching process of the silicon wafer mask that was used to prepare the PDMS mold [52].

3.2. Wettability of cPEVA substrates

The present microstructured cPEVA substrates were macroscopically analyzed by dCA measurements. First, the microstructured surface was analyzed by the sessile drop method with water (Fig. 2a) showing a CA of $114 \pm 2°$ and thus, can be classified as a hydrophobic material (Table S1). To investigate the influence of the micro and nano surface topography on the CA, a flat cPEVA film with $S_a < 1$ nm was prepared and explored as a reference material surface. The CA of the flat cPEVA surface is significantly lower ($97 \pm 4°$) compared to the CA of the microstructured cPEVA substrate (Fig. 2b, Table S1) and in good agreement with the results reported for PEVA with the same vinyl acetate content [48]. The impalement scenario of the water drop related to the Wenzel state is suggested for the wetting behavior of the present surface. This is further supported by comparing the CA hysteresis showing a significant increase from the flat ($21 \pm 5°$) to the structured surface ($43 \pm 4°$) that clearly accounts for the increase in the surface roughness. To check experimentally for influences of nanostructure on the CA, the cylinders were investigated by dynamic μ-CA measurements via environmental scanning electron microscopy (ESEM), revealing a μ-CA of $101 \pm 5°$ on the nanorough (S_a up to 10 nm) cylinder's top surface (Fig. 2c) and $93 \pm 3°$ on the nanosmooth ($S_a < 1$ nm) interspace surface for condensing water droplets (Fig. 2d). This indicates that the nanoroughness slightly increases the μ-CA on the present structure and it can be anticipated that the observed macroscopic effect can be predominantly attributed to the changes in the microcylinder height. To explore the aerophilic/aerophobic behavior of the surface and the influence of the topography, the cPEVA films were immersed in water and analyzed by the captive bubble method. In contrast to the sessile drop method, here a dramatic difference in CA of temporarily flat cPEVA ($110 \pm 2°$) and structured cPEVA ($36 \pm 2°$) substrates was observed (Fig. 2f, g). For both substrates the CA was constant (variation $\leq \pm 5°$) over the measured temperature range from 25 °C to 75 °C, which confirmed that no chemical or topographical alterations occur at the material surface upon heating (Fig. 2e, Tables S2, S3).

The flat cPEVA surface can be classified as an aerophilic material, while the structured surface acts aerophobic, which stays in contrast to the hydrophobic nature observed for both surfaces by the sessile drop method (Fig. 2a, b). This behavior for the structured cPEVA substrate can be explained by a water film covering the interspace between the microstructures of the substrate and air bubble dominating the interface interaction. This is indicated by the different interface refraction in Fig. 2g (structured surfaces) compared to Fig. 2f (flat surface). This is supported by the comparison of the CA hysteresis showing an opposite
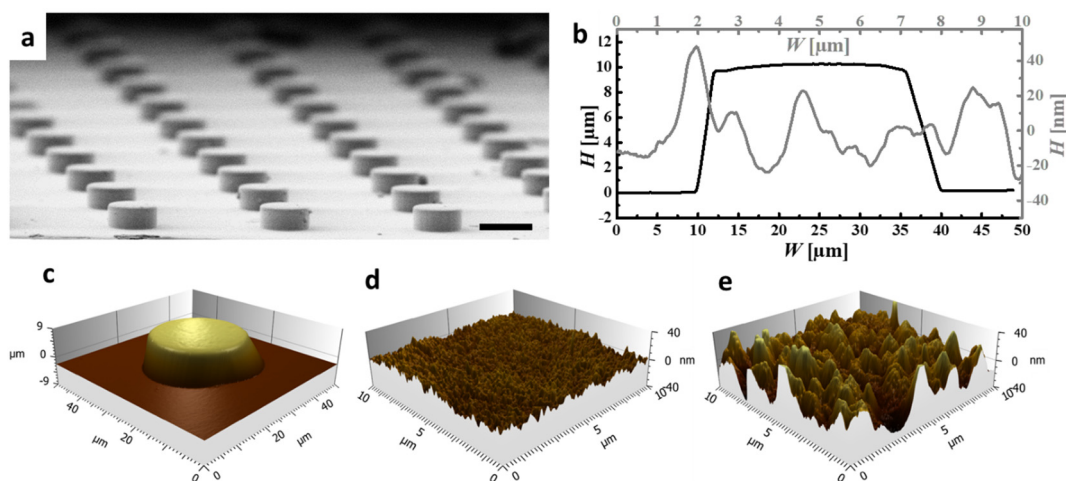
Fig. 1. Surface characterization of the microcylindered cPEVA substrate: (a) SEM image of the surface showing regular cylinder arrays (scale bar 25 μm), (b) height profile of the cylinder shape (black) and cylinder's top surface (grey); 3D reconstruction of AFM scans of a single microcylinder (c), surface roughness at the cylinder interspace (d) and the cylinder's top surface (e). The vertical axes of AFM 3D height images are −9 μm to 9 μm for (c), and −40 nm to 40 nm for (d) and (e).

trend compared to the sessile drop method. The original flat surface showed values of $16 \pm 2°$ (Table S2), while the structured cPEVA showed similar values of $13 \pm 2°$ (Table S3). With the assumption, that just the cylinders top surface represents solid-air contact, > 90% of the theoretical contact area of the air bubble is water, which explains the apparent aerophobic surface behavior.

3.3. Characteristics of programmed cPEVA substrates

For crosslinked semicrystalline polymers, the fixation of a temporary shape relies on the crystallization of switching domains at the fixation temperature (T_{fix}), that have been in the rubbery state at T_{prog} [34]. To investigate the influence of T_{prog} on temporary topographies, the microstructured cPEVA films were compressed at five different deformation temperatures T_{prog} ranging from $T_{prog} = 40$ °C to $T_{prog} = 100$ °C. The obtained temporary surfaces were analyzed by optical microscopy showing a uniform vertical deformation over large cylinder arrays (Fig. S3). In addition, the cylinder height was analyzed by SEM supporting uniform height compression of cylinders over large arrays (exemplified for $T_{prog} = 40$ °C in Fig. S4). The AFM height images on micro- and nanoscale as well as corresponding height profiles for different T_{prog} are given in Fig. 3, and the geometrical sizes and deformation ratios (R_d) are listed in Table 1.

On the microscale, the programmed cylinders demonstrate reduced heights and increased diameters compared to the original microcylinder upon increased T_{prog}. This trend is in accordance with the assumption that the amount of recrystallizing polymers and hence the fixation ability increases by T_{prog} which hinders the entropy-driven recovery of the cylinder upon pressure release [37]. At T_{prog} of 70 °C, the fixed cylinder height almost equals the surrounding surface

corresponding to an apparent deformation ratio of 94%. Interestingly, for T_{prog}s of 100 °C and 80 °C negative heights of up to 400 nm were measured when compared to the surrounding surface, showing a microwell topography. This might be explained by the fact that at higher temperatures almost all polyethylene crystals are molten, which recrystallize in an oriented fashion during cooling under stress and thus cause spatial shrinkages resulting in the formation of microcavities [54].

On the nanoscale, the cylinder's top roughness is reduced upon increasing T_{prog} showing roughness around S_a ~1 nm at 100 °C with similar deformation ratios as obtained for the cylinder height (Table 1). The results show that cPEVA can be programmed on both, nano- and microscale.

3.4. Temperature-memory performance of programmed cPEVA substrates

The height recovery of the programmed cylinders was observed by optical microscopy as the sample was heated stepwise from 25 °C to 100 °C and was allowed to equilibrate at each temperature for 10 min prior measurement. As depicted in Fig. S3, the recovery of the cylinders was homogeneous and vertical to the surface over large cylinder areas for all T_{prog}. Following the same stepwise heating protocol, the recovery was monitored by AFM to characterize the height and top surface roughness evolution of a single cylinder. The recovery is exemplified in Fig. 4a showing homogeneous shape and top surface roughness recovery of the sample programmed at 70 °C. By increasing the temperature, the apparent height of the cylinder increased while the diameter decreased reaching the values of the original cylinder geometry at 100 °C (Fig. 4a, top row). Simultaneously the cylinder's top surface roughness recovers to the value of the original cylinder's top surface (Fig. 4a, bottom row). The shape and top surface roughness recovery evolution

Table 1
AFM height and roughness data, deformation ratios (R_d) and recovery ratios (R_r) of single cylinders (micro) and cylinder's top surface roughness (nano) of programmed surfaces.

T_{prog} [°C]		40	60	70	80	100	Original
Micro	D [μm]	30.4 ± 0.1	30.6 ± 0.1	31.8 ± 0.2	34.1 ± 0.1	33.9 ± 0.1	25.0 ± 0.2
	H [μm]	4.80 ± 0.02	1.32 ± 0.02	0.63 ± 0.03	-0.41 ± 0.02	-0.13 ± 0.03	10.5 ± 0.3
	$R_{d,\mu}$ [%]	54 ± 1	87 ± 1	94 ± 1	104 ± 1	101 ± 1	–
	$R_{r,\mu}$ [%]	113 ± 1	104 ± 1	103 ± 1	98 ± 1	101 ± 1	–
	$T_{sw,\mu}$	41 ± 2	61 ± 2	67 ± 2	79 ± 2	78 ± 2	–
Nano	S_a[a] [nm]	5.0 ± 0.2		1.0 ± 0.2		1.0 ± 0.3	10.0 ± 1.0
	$R_{d,n}$ [%]	51 ± 1		88 ± 1		91 ± 1	–
	$R_{r,n}$ [%]	100 ± 1		97 ± 1		96 ± 1	–
	$T_{sw,n}$	38 ± 2		66 ± 2		81 ± 2	–

[a] The surface roughness S_a was calculated according to Eq. (1), the deformation/recovery ratios $R_{x,y}$ were calculated according to Eqs. (2)–(5).
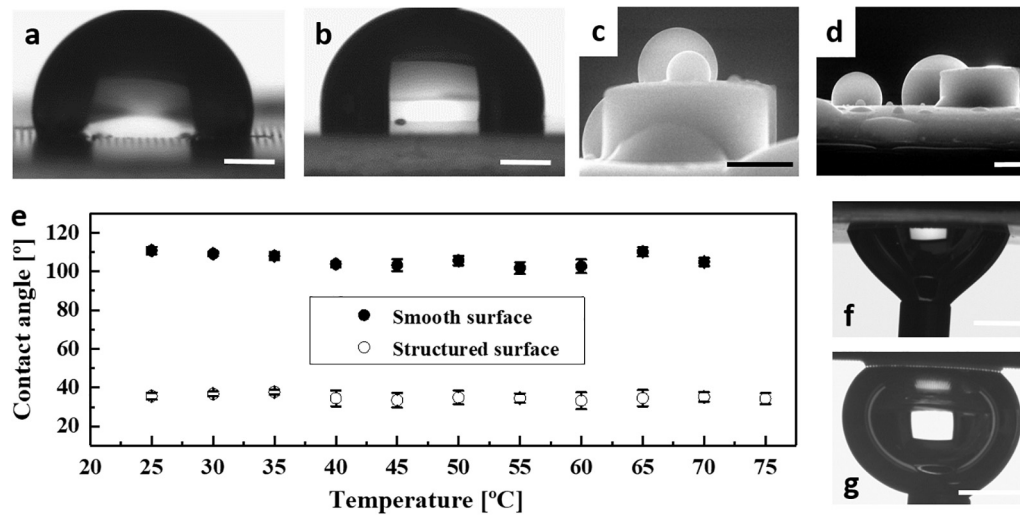
Fig. 2. Wettability of the cPEVA surface: Optical images of the CA measurements by the sessile drop method for the structured surface (a) and flat surface (b); SEM images of μ-CA measurement on cylinder's top surface (c) and on the intercylinder surface (d); Diagram of the temperature-dependent CA measured via captive bubble method (e) and optical images of representative captive bubble measurements on flat surface (f) and structured surface (g). Scale bar is 25 μm in (c), (d) and 0.5 mm in (a), (b), (f) and (g).

for the other T_{prog} are given in Fig. S5, S6, while corresponding values of height and top surface roughness are depicted in Tables S4, S6. The corresponding temperature dependency of shape and top surface roughness recovery are visualized in height-temperature diagrams (Fig. 4b) and roughness-temperature diagrams (Fig. 4c) suggesting continuous recovery on both nano- and microscale for samples deformed at different T_{prog}. Independent from T_{prog}, the cylinders and top surface roughness recover to the original height (Table S4) and original top surface roughness (Table S6) with high corresponding recovery ratios (R_r) of ≥98% at 100 °C (Table S5). This indicates that the shape recovery capability is excellent and not altered by changing the T_{prog} as described previously [37].

However, although the programmed cylinders at 40 °C and 60 °C are almost completely recovered at 50 °C and 70 °C, respectively, the height is not reaching a plateau but is still increasing slowly until 100 °C (Fig. 4b, c). This might be ascribed to the fact that the shape fixation is contributed by recrystallization of amorphous fixation domains as

well as deformation of crystals existing at low T_{prog} during compression [55]. In the present case, deformation of crystals is pronounced at low T_{prog} as the cylinders experience higher stresses since it lacks compensation of compression stress by material deformation into the substrate compared to high T_{prog}. This may result in local fragmentation of large crystals during programming as it was observed in case of the macroscopic programming of cPEVA by uniaxial elongation [41]. The height-temperature curves also show that increasing T_{prog} is correlated with a shape recovery shift to higher temperatures as it is reported for macroscopic shape recovery of cPEVA [37]. This temperature-memory effect relies mainly on the dependency of melting temperature on crystal size, showing a suppression for nano-sized polymer crystals [56]. The higher T_{prog} larger are the crystals formed during recrystallization due to higher mobility of the polymer chains. This leads to an increase of T_m of the crystals of the fixation domains resulting in the recovery shift to higher temperatures. To quantify this trend, the switching temperatures (T_{sw}) were determined as the inflection points of the
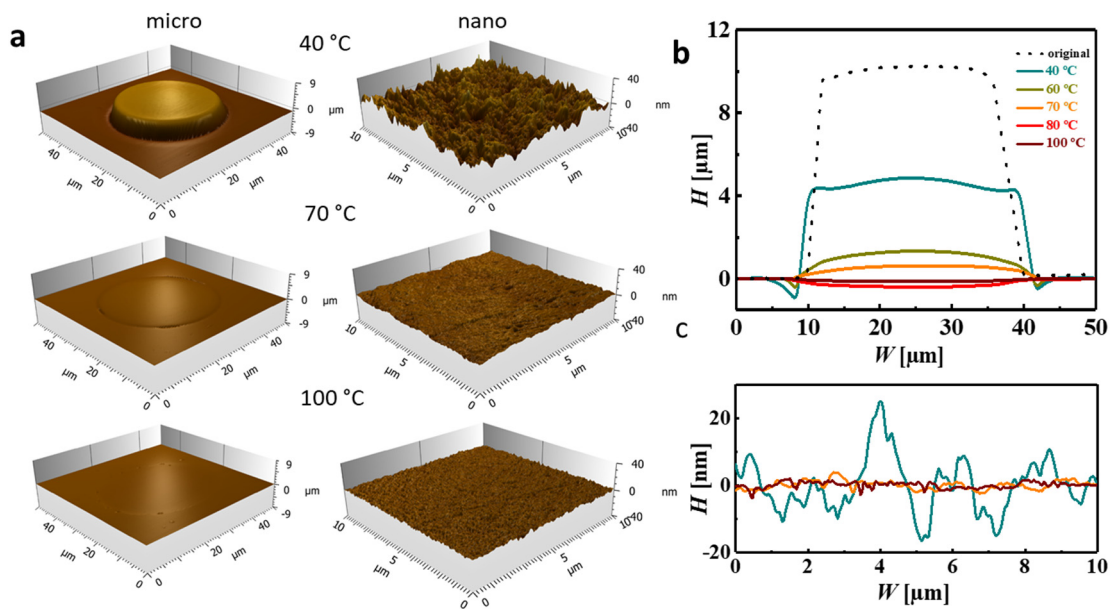

Fig. 3. AFM characterization of single cylinders on programmed surfaces: (a) 3D models of AFM height scanning of cylinder shape (micro, vertical axis from −9 μm to 9 μm) and cylinder's top surface (nano, vertical axis from −40 nm to 40 nm) at representative programming temperatures of 40 °C, 70 °C and 100 °C; (b) Height profile of cylinders for different programming temperatures compared to the original cylinder height (dashed line) and (c) height profile of the cylinders' top surface for different programming temperatures.
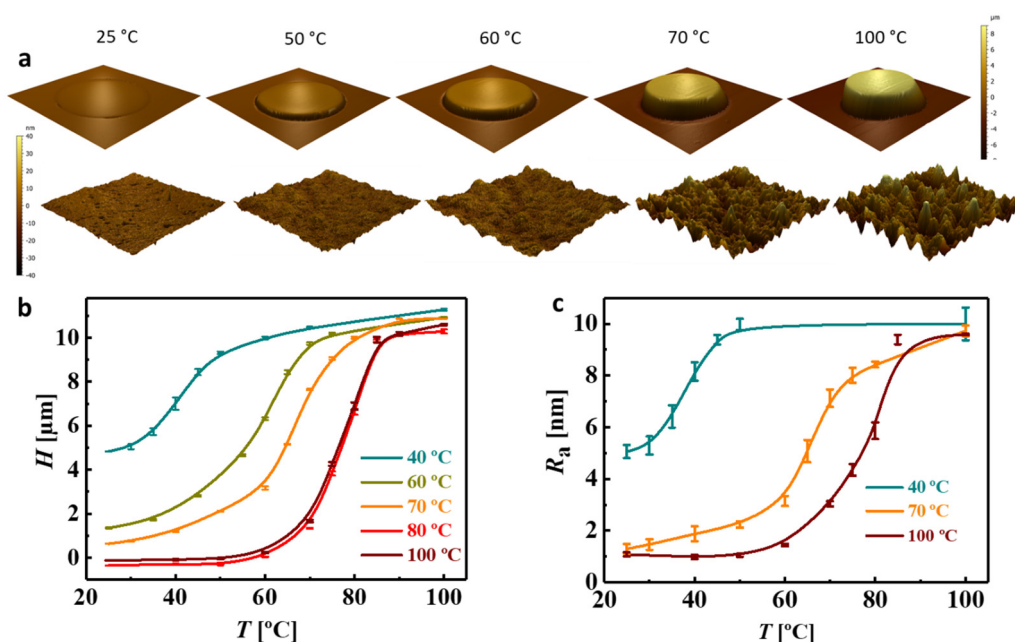
Fig. 4. AFM characterization of single cylinders height evolution during recovery: (a) 3D reconstruction of AFM scans of single cylinder during stepwise heating on micro (top row) and cylinder's top surface on nano roughness (bottom row) for representative samples programmed at 70 °C; (b) Diagram showing the height evolution of cylinder in dependence of temperature for different programming temperatures and (c) diagram showing the nanoroughness of the cylinders' top surfaces by temperature for programmed cylinders at 40 °C, 70 °C and 100 °C.

recovery-temperature curves representing the temperatures of highest shape recovery rate (Fig. 4b, c). A systematic increase of T_{sw} from 41 ± 2 °C (for $T_{prog} = 40$ °C) to 79 ± 2 °C for the samples programmed at 80 °C were observed on the microscale as well as on the nanoscale. Thereby, the switching temperatures equal the T_{prog}. However, T_{sw} is almost constant for samples of $T_{prog} \geq 80$ °C. This might be related to the fact that at 80 °C all polyethylene crystals are molten, which is reflected in the DSC curve (Fig. S1). The AFM investigation showed that the cylinders recover almost simultaneously on both micro- and nano level upon heating, whereby the switching temperature (T_{sw}) can be controlled by the T_{prog}.

3.5. Temperature-induced switching of aerophobicity

Based on the confirmed tailorable switch of surface topography on both nano- and micro-level by temperature, the surface wettability as related macroscopic surface function was analyzed via in-situ temperature dCA experiments using the captive bubble method. Therefore, the water was heated stepwise from 25 °C to 75 °C before an air bubble was brought in contact to the surface. The dCA data of the programmed samples are given in Tables S7, S8, S9. As depicted in Fig. 5a, c, the substrate programmed at $T_{prog} = 40$ °C showed CAs of $96 \pm 2°$ at 25 °C representing aerophilic/hydrophobic behavior that can be described
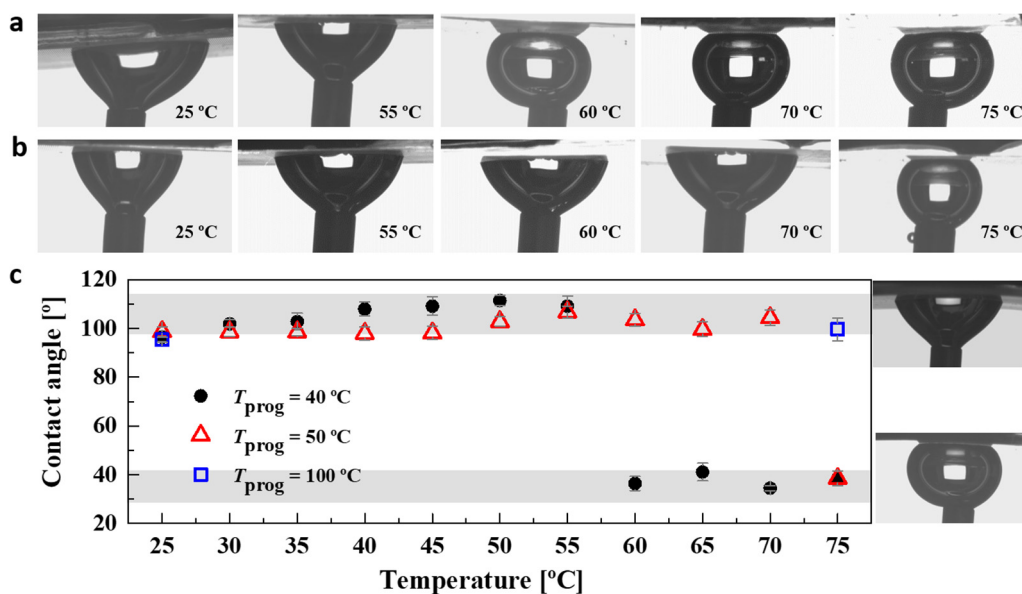

Fig. 5. In-situ CA measurements during surface recovery via captive bubble method: Optical images of the captive bubble evolution during surface recovery for the sample programmed at 40 °C (a) and 50 °C (b); (c) Diagram showing the dependency of CA in dependence of recovery temperature for programmed samples at 40 °C, 50 °C and 100 °C with representative optical images according to the flat (upper right) and microstructured, surface (bottom right). The outer diameter of the needle is 0.5 mm.

theoretically by the Wenzel state. In comparison, the original flat surface showed similar wetting behavior over the temperature range from 25 °C to 75 °C (Fig. 2e) represented as the upper grey area in Fig. 5c. The wettability for other temporary surfaces is similar (~95°) as it is depicted in Tables S8 and S9 suggesting that the wettability of the programmed surfaces is independent of T_{prog}. In the following online heating process, the recovering surface demonstrated slightly increasing CA until 55 °C with CA = 109 ± 4° that can be attributed to the increase of micro- and nanoroughness upon recovery. However, at 60 °C a large decrease in CA = 36 ± 3° was observed that represents the wettability switch from aerophilic to aerophobic with similar air bubble CAs as the original microstructured surface (bottom grey area, Fig. 5c). This can be explained by water trapped in the intercylinder space resulting in an apparent hydrophilic surface (see Section 3.2).

In accordance with the height recovery at 60 °C derived from in-situ AFM (Fig. 4b), this correlates to a cylinder height of 9.9 ± 0.1 μm representing almost full height recovery (Table S4). Hence, the cylinder height threshold for the wettability switch is 10 μm, (the original microcylinder height) for the present surface geometry and air bubble size. The switch in wettability occurs at higher temperatures when compared to the T_{sw} determined in AFM experiments. Consequently, for samples programmed at $T_{prog} = 100$ °C no switch could be observed within the experimental conditions for the online investigations limited to a water temperature of 75 °C (Fig. 5c). However, after offline heating to 100 °C for all samples complete recovery was obtained, which was documented by an aerophobic behavior (CA in the range of 34° to 39°) similar to that observed for the original microstructured cPEVA substrate (Tables S7, S8, S9). To prove that the aerophobicity switch can be tailored by variation of T_{prog} a sample programmed at 50 °C was investigated showing the wettability switch at 75 °C within the online experiment.

Based on the proven switch of aerophobicity, the in-situ temperature dCA experiments were used with a modified setup to test the principle of air bubble adhesion/repellence on the surface (Fig. 6). Therefore, the sample programmed at 40 °C was mounted with the structured side facing upwards and air bubbles were allowed to attach from above to the surface at a certain temperature in the range from 25 °C to 75 °C. The bubble before attaching was larger than 0.5 mm in diameter. As a reference, the original flat cPEVA substrate was tested showing an air

bubble attachment independent from temperature, while the original microstructured cPEVA showed air bubble repellence (Fig. S7). By using the temporary surface programmed at 40 °C, the surface adheres the air bubble until repellence starting from 55 °C (see also SI Videos 1 and 2). The air bubble repellence seems to start earlier than the switch in CA (60 °C), which might be due to the bubble's buoyancy and the different air bubble sizes prior contacting the surface.

4. Conclusions

A thermally-induced switch in underwater aerophobicity and thus, on demand air bubble repellence on programmed cPEVA substrates was achieved by recovering a well-defined surface topography. Here, the recovered microcylinders allow trapping of a water film at the cylinder interspace, which then dominates the interaction with approaching air bubbles and in this way generates the aerophobic behavior of the hydrophobic material. The associated increase in nanoroughness at the cylinders top surface is further supporting the switch in aerophobicity. The related switching temperatures could be adjusted in the range from 58 ± 3 °C to 73 ± 3 °C by solely physical means via variation of the deformation temperature applied during the temperature-memory creation procedure. It is anticipated that the presented on-demand gas bubble repellence technology, which was demonstrated for hydrophobic polymers exposed to millimeter sized air bubbles underwater, might be extended to a switchable superaerophobic behavior, capable of removing or capturing micro gas bubbles, by adapting the geometries of both micro- and nanofeatures. This approach to switching the underwater gas bubble wettability of hydrophobic polymeric substrates by topographical changes without altering the materials chemistry could be attractive for the design of smart (bio)sensor materials.

Supplementary data to this article can be found online at https://doi.org/10.1016/j.matdes.2018.12.002.
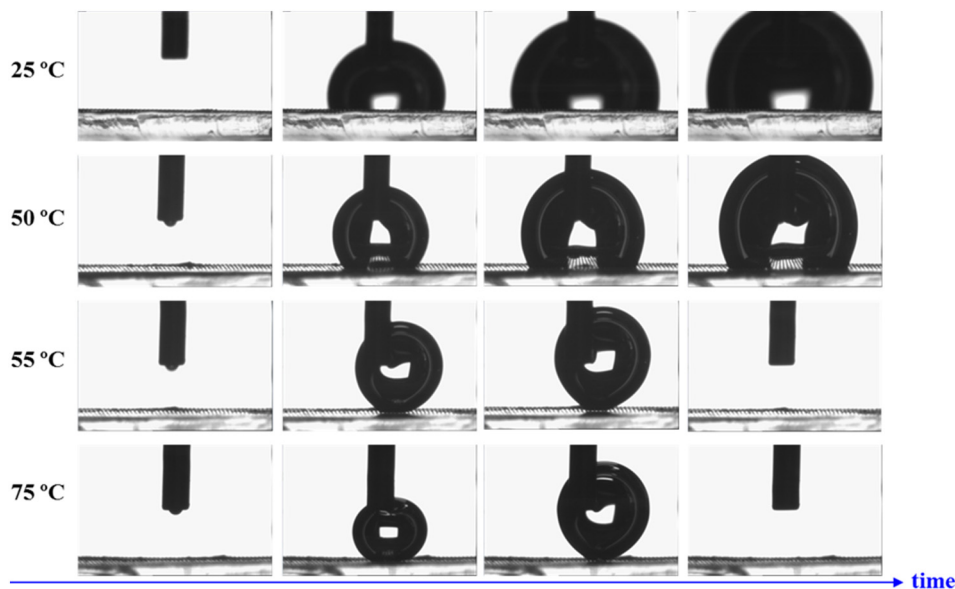
Fig. 6. Optical images of the temperature-dependent bubble-to-surface attachment evolution during surface recovery showing an adhesion-repellence switch between 50 °C and 55 °C for the surface programmed at 40 °C. The outer diameter of the needle is 0.5 mm.

Data availability

The raw/processed data required to reproduce these findings cannot be shared at this time as the data also forms part of an ongoing study.

CRediT authorship contribution statement

CRediT authorship contribution statement

Acknowledgements

References

[1] J. Yong, F. Chen, W. Li, J. Huo, Y. Fang, Q. Yang, H. Bian, X. Hou, Underwater superaerophobic and superaerophilic nanoneedles-structured meshes for water/bubbles separation: removing or collecting gas bubbles in water, Glob. Chall. 2 (4) (2018) 1700133.

[2] C. Yu, P. Zhang, J. Wang, L. Jiang, Superwettability of gas bubbles and its application: from bioinspiration to advanced materials, Adv. Mater. 29 (45) (2017), 1703053.

[3] A. Marmur, Soft contact: measurement and interpretation of contact angles, Soft Matter 2 (1) (2006) 12–17.

[4] Y. Tian, B. Su, L. Jiang, Interfacial material system exhibiting superwettability, Adv. Mater. 26 (40) (2014) 6872–6897.

[5] J. Drelich, E. Chibowski, Superhydrophilic and superwetting surfaces: definition and mechanisms of control, Langmuir 26 (24) (2010) 18621–18623.

[6] R.N. Wenzel, Resistance of solid surfaces to wetting by water, Ind. Eng. Chem. 28 (8) (1936) 988–994.

[7] A.B.D. Cassie, S. Baxter, Wettability of porous surfaces, Trans. Faraday Soc. 40 (0) (1944) 546–551.

[8] L. Gao, T.J. McCarthy, How Wenzel and Cassie were wrong, Langmuir 23 (7) (2007) 3762–3765.

[9] C. Dorrer, J. Rühe, Superaerophobicity: repellence of air bubbles from submerged, surface-engineered silicon substrates, Langmuir 28 (42) (2012) 14968–14973.

[10] J. Kamei, Y. Saito, H. Yabu, Biomimetic ultra-bubble-repellent surfaces based on a self-organized honeycomb film, Langmuir 30 (47) (2014) 14118–14122.

[11] L. Mammen, K. Bley, P. Papadopoulos, F. Schellenberger, N. Encinas, H.-J. Butt, C.K. Weiss, D. Vollmer, Functional superhydrophobic surfaces made of Janus micropillars, Soft Matter 11 (3) (2015) 506–515.

[12] P. Papadopoulos, B.-E. Pinchasik, M. Tress, D. Vollmer, M. Kappl, H.-J. Butt, Wetting of soft superhydrophobic micropillar arrays, Soft Matter 14 (36) (2018) 7429–7434.

[13] S. Prasha, C. Anirban, G. Varun, L. Cheng, Controllable strain recovery of shape memory polystyrene to achieve superhydrophobicity with tunable adhesion, J. Micromech. Microeng. 24 (11) (2014), 115006.

[14] C. Shi, X. Cui, X. Zhang, P. Tchoukov, Q. Liu, N. Encinas, M. Paven, F. Geyer, D. Vollmer, Z. Xu, H.-J. Butt, H. Zeng, Interaction between air bubbles and superhydrophobic surfaces in aqueous solutions, Langmuir 31 (26) (2015) 7317–7327.

[15] J.M. Wang, Q.L. Yang, M.C. Wang, C. Wang, L. Jiang, Rose petals with a novel and steady air bubble pinning effect in aqueous media, Soft Matter 8 (7) (2012) 2261–2266.

[16] J.E. George, V.R.M. Rodrigues, D. Mathur, S. Chidangil, S.D. George, Self-cleaning superhydrophobic surfaces with underwater superaerophobicity, Mater. Des. 100 (2016) 8–18.

[17] C. Shan, J. Yong, Q. Yang, F. Chen, J. Huo, J. Zhuang, Z. Jiang, X. Hou, Reversible switch between underwater superaerophilicity and superaerophobicity on the superhydrophobic nanowire-haired mesh for controlling underwater bubble wettability, AIP Adv. 8 (4) (2018), 045001.

[18] Y. Jiao, C. Li, S. Wu, Y. Hu, J. Li, L. Yang, D. Wu, J. Chu, Switchable underwater bubble wettability on laser-induced titanium multiscale micro-/nanostructures by vertically crossed scanning, ACS Appl. Mater. Interfaces 10 (19) (2018) 16867–16873.

[19] M.A.C. Stuart, W.T.S. Huck, J. Genzer, M. Müller, C. Ober, M. Stamm, G.B. Sukhorukov, I. Szleifer, V.V. Tsukruk, M. Urban, F. Winnik, S. Zauscher, I. Luzinov, S. Minko, Emerging applications of stimuli-responsive polymer materials, Nat. Mater. 9 (2010) 101.

[20] D. Liu, D.J. Broer, Responsive Polymer Surfaces: Dynamics in Surface Topography, Wiley-VCH Verlag GmbH & Co. KGaA, 2017.

[21] M. Wei, Y. Gao, X. Li, M.J. Serpe, Stimuli-responsive polymers and their applications, Polym. Chem. 8 (1) (2017) 127–143.

[22] T. Lv, Z. Cheng, D. Zhang, E. Zhang, Q. Zhao, Y. Liu, L. Jiang, Superhydrophobic surface with shape memory micro/nanostructure and its application in rewritable chip for droplet storage, ACS Nano 10 (10) (2016) 9379–9386.

[23] L. Zhao, J. Zhao, Y. Liu, Y. Guo, L. Zhang, Z. Chen, H. Zhang, Z. Zhang, Continuously tunable wettability by using surface patterned shape memory polymers with giant deformability, Small 12 (24) (2016) 3327–3333.

[24] J.K. Park, S. Kim, Droplet manipulation on a structured shape memory polymer surface, Lab Chip 17 (10) (2017) 1793–1801.

[25] W.L. Lee, H.Y. Low, Geometry- and length scale-dependent deformation and recovery on micro- and nanopatterned shape memory polymer surfaces, Sci. Rep. 6 (2016), 23686.

[26] N. Garcia-Huete, J.M. Cuevas, J.M. Laza, J.L. Vilas, L.M. Leon, Polymeric shape-memory micro-patterned surface for switching wettability with temperature, Polymers-Basel 7 (9) (2015) 1674–1688.

[27] S.A. Turner, J. Zhou, S.S. Sheiko, V.S. Ashby, Switchable micropatterned surface topographies mediated by reversible shape memory, ACS Appl. Mater. Interfaces 6 (11) (2014) 8017–8021.

[28] Y. Han, Y. Liu, W. Wang, J. Leng, P. Jin, Controlled wettability based on reversible micro-cracking on a shape memory polymer surface, Soft Matter 12 (10) (2016) 2708–2714.

[29] D. Zhang, Z. Cheng, H. Kang, J. Yu, Y. Liu, L. Jiang, A smart superwetting surface with responsivity in both surface chemistry and microstructure, Angew. Chem. Int. Ed. 57 (14) (2018) 3701–3705.

[30] E. Lee, S. Yang, Bio-inspired responsive polymer pillar arrays, MRS Commun. 5 (2) (2015) 97–114.

[31] Y.-J. Kim, Y.T. Matsunaga, Thermo-responsive polymers and their application as smart biomaterials, J. Mater. Chem. B 5 (23) (2017) 4307–4321.

[32] F. Xia, L. Jiang, Bio-inspired, smart, multiscale interfacial materials, Adv. Mater. 20 (15) (2008) 2842–2858.

[33] L. Sun, W.M. Huang, T.X. Wang, H.M. Chen, C. Renata, L.W. He, P. Lv, C.C. Wang, An overview of elastic polymeric shape memory materials for comfort fitting, Mater. Des. 136 (2017) 238–248.

[34] A. Lendlein, S. Kelch, Shape-memory polymers, Angew. Chem. Int. Ed. 41 (12) (2002) 2034–2057.

[35] W.G. Bae, J.H. Choi, K.Y. Suh, Pitch-tunable size reduction patterning with a temperature-memory polymer, Small 9 (2) (2013) 193–198.

[36] Y. Jiang, L. Fang, K. Kratz, A. Lendlein, Influence of compression direction on the shape-memory effect of micro-cylinder arrays prepared from semi-crystalline polymer networks, MRS Adv. 1 (27) (2016) 1985–1993.

[37] K. Kratz, S.A. Madbouly, W. Wagermaier, A. Lendlein, Temperature-memory polymer networks with crystallizable controlling units, Adv. Mater. 23 (35) (2011) 4058–4062.

[38] P. Miaudet, A. Derre, M. Maugey, C. Zakri, P.M. Piccione, R. Inoubli, P. Poulin, Shape and temperature memory of nanocomposites with broadened glass transition, Science 318 (5854) (2007) 1294–1296.

[39] T. Xie, K.A. Page, S.A. Eastman, Strain-based temperature memory effect for Nafion and its molecular origins, Adv. Funct. Mater. 21 (11) (2011) 2057–2066.

[40] G. Li, A. Wang, Cold, warm, and hot programming of shape memory polymers, J. Polym. Sci. B Polym. Phys. 54 (14) (2016) 1319–1339.

[41] U. Nochel, C.S. Reddy, K. Wang, J. Cui, I. Zizak, M. Behl, K. Kratz, A. Lendlein, Nanostructural changes in crystallizable controlling units determine the temperature-memory of polymers, J. Mater. Chem. A 3 (16) (2015) 8284–8293.

[42] L. Sun, W.M. Huang, Mechanisms of the multi-shape memory effect and temperature memory effect in shape memory polymers, Soft Matter 6 (18) (2010) 4403–4406.

[43] A.M. Henderson, Ethylene-vinyl acetate (EVA) copolymers: a general review, IEEE Electr. Insul. Mag. 9 (1) (1993) 30–38.

[44] S. Giri, C. Wan, Electronic applications of ethylene vinyl acetate and its composites, in: D. Ponnamma, K.K. Sadasivuni, C. Wan, S. Thomas, M. Al-Ali AlMa'adeed (Eds.), Flexible and Stretchable Electronic Composites, Springer International Publishing, Cham 2016, pp. 61–85.

[45] C. Schneider, R. Langer, D. Loveday, D. Hair, Applications of ethylene vinyl acetate copolymers (EVA) in drug delivery systems, J. Control. Release 262 (2017) 284–295.

[46] J.A. Soto Puente, K. Fatyeyeva, C. Chappey, S. Marais, E. Dargent, Layered poly(ethylene-co-vinyl acetate)/poly(ethylene-co-vinyl alcohol) membranes with enhanced water separation selectivity and performance, ACS Appl. Mater. Interfaces 9 (7) (2017) 6411–6423.

[47] I.O. Ucar, M.D. Doganci, C.E. Cansoy, H.Y. Erbil, I. Avramova, S. Suzer, Combined XPS and contact angle studies of ethylene vinyl acetate and polyvinyl acetate blends, Appl. Surf. Sci. 257 (22) (2011) 9587–9594.

[48] M.D. Doganci, C.E. Cansoy, I.O. Ucar, H.Y. Erbil, E. Mielczarski, J.A. Mielczarski, Combined XPS and contact angle studies of flat and rough ethylene-vinyl acetate copolymer films, J. Appl. Polym. Sci. 124 (3) (2011) 2100–2109.

[49] T. Carlsson, P. Konttinen, U. Malm, P. Lund, Absorption and desorption of water in glass/ethylene-vinyl-acetate/glass laminates, Polym. Test. 25 (5) (2006) 615–622.

[50] M. Behl, K. Kratz, U. Noechel, T. Sauter, A. Lendlein, Temperature-memory polymer actuators, P. Natl. Acad. Sci. U.S.A. 110 (31) (2013) 12555–12559.

[51] J.J. Li, W.R. Rodgers, T. Xie, Semi-crystalline two-way shape memory elastomer, Polymer 52 (23) (2011) 5320–5325.

[52] Y. Liu, M.Y. Razzaq, T. Rudolph, L. Fang, K. Kratz, A. Lendlein, Two-level shape changes of polymeric microcuboids prepared from crystallizable copolymer networks, Macromolecules 50 (6) (2017) 2518–2527.

[53] J.D. Eisenhaure, T. Xie, S. Varghese, S. Kim, Microstructured shape memory polymer surfaces with reversible dry adhesion, ACS Appl. Mater. Interfaces 5 (16) (2013) 7714–7717.

[54] S. Matsuoka, Pressure-induced crystallization in polyethylene, J. Polym. Sci. 42 (140) (1960) 511–524.

[55] Z. Bartczak, R.E. Cohen, A.S. Argon, Evolution of the crystalline texture of high-density polyethylene during uniaxial compression, Macromolecules 25 (18) (1992) 4692–4704.

[56] Q. Jiang, C.C. Yang, J.C. Li, Size-dependent melting temperature of polymers, Macromol. Theory Simul. 12 (1) (2003) 57–60.